

Quasitrapped modes in metasurfaces of anisotropic MoS₂ nanoparticles for absorption and polarization control in the telecom wavelength range

Alexei V. Prokhorov,^{1,2,*} Alexander V. Shesterikov,^{1,2} Mikhail Yu. Gubin^{1,2},,^{1,2} Valentyn S. Volkov,² and Andrey B. Evlyukhin³

¹*Department of Physics and Applied Mathematics, Vladimir State University named after A. G. and N. G. Stoletovs, Vladimir, Russia*

²*Center for Photonics and 2D Materials, Moscow Institute of Physics and Technology, Dolgoprudny, Russia*

³*Institute of Quantum Optics, Leibniz Universität Hannover, Hannover, Germany*



(Received 4 January 2022; revised 29 June 2022; accepted 1 July 2022; published 14 July 2022)

Resonant optical responses of anisotropic molybdenum disulfide (MoS₂) nanoparticles (NPs) and their two-dimensional arrays (metasurfaces) are investigated. The nanoparticles in the form of disks with holes and with MoS₂ layers oriented perpendicular to the disk's basis (in-plane material anisotropy) are considered. Using numerical calculations with analytical multipole analysis, we show that the material anisotropy of NPs provides an additional degree of freedom for manipulation of their resonant magnetic and electric dipole responses and affect the effective dipole polarizabilities. Based on this possibility and applying a special tuning procedure, we construct the MoS₂ metasurfaces supporting the quasitrapped mode (QTM) resonance around the telecom wavelength of 1550 nm with high quality factor and high sensitivity to the environment. It is shown that regardless of extremely weak absorption of the single nanoparticles, the excitation of the QTM leads to effective narrowband absorption in the telecom wavelength range depending on the polarization direction of normally incident waves. It is demonstrated that a metasurface, composed of the MoS₂ disks with the in-plane material anisotropy, has the properties of a continuous birefringent medium. Due to these properties, a normally incident linearly polarized wave can be transformed into transmitted and reflected waves with changed polarizations.

DOI: [10.1103/PhysRevB.106.035412](https://doi.org/10.1103/PhysRevB.106.035412)

I. INTRODUCTION

Currently, the design of the ultranarrowband absorbers is of great practical interest. Until recently, the structures and metasurfaces based on conductive materials have been used to create such absorbers. Their configuration and lattice resonances [1,2] allow narrowing the spectral transmission window, while the conductor provides fast damping of light [3–6]. The composite metal-dielectric absorbers utilize the resonances of a dielectric metamaterial to concentrate light and direct it to a plasmonic substrate for conversion of near field energy to Joule losses [7]. The quality factor of the considered resonances as the ratio of the resonant wavelength to the full width at half maximum (FWHM) depends on the topology of the structure. For example, in Ref. [5], the quality factor of about 130 was achieved in the near-infrared range for gold mushrooms on a complex substrate; in the theoretical work [6] for an array of gold nanoribbons on a thin gold layer, it reaches 350 in the visible range. In addition, the terahertz absorbers based on the structured graphene [8] with a quality factor of about 9 and with a quality factor of about several hundred units [9] for a wavelength 1550 nm were proposed. An additional remarkable feature of narrowband absorbers is high sensitivity to the local environment, which allows for detection of individual particles and nano-objects with high precision [10–13]. However, the obligatory presence of a plasmonic substrate in such structures does not allow

creating functional metacoatings on their basis deposited on the surfaces with arbitrary shapes. The solution can be the use of absorption properties of individual nanoparticles enhanced in a narrow spectral range due to interference effects in the lattice. In this case, the diffractive-coupled lattice of metal or semiconductor NPs provides the collective lattice resonances with the quality factors determined by the configuration and size parameters of the system [14–19].

The recent researches have focused on the development of all-dielectric absorbers and sensors, for which a high level of absorption is achieved by matching impedances and combining electric and magnetic dipole resonances at the same frequency in a metamaterial fabricated from weakly absorbing NPs, for example, solid Si NPs [20,21]. However, the quality factor of such systems is low and does not exceed 12. Not very high quality factor values are reached in metasurfaces composed of doped Si [22,23] or Ge [24] building blocks with increased material losses.

The improvement of the quality factor control of the all-dielectric absorbers and enhancing sensitivity of the corresponding sensors can be reached, on the one hand, by applying a new physical mechanism and, on the other hand, by using new optical materials for their fabrication. One such approach is to combine the fundamental effects of nonlocality in individual NPs optical response and the collective resonances of metasurfaces and nanostructures composed of such building blocks [25–28]. It should be noted that the problem of localization and nondiffractive propagation of surface waves in all-dielectric metasurfaces has already been considered earlier using the Si slab gratings with combination of hyperboliclike

*avprokhorov33@mail.ru

and elliptic dispersion regimes [29]. At the same time, the use of new materials and other physical effects can significantly extend the scope of such structures [30]. In particular, the metasurface composed of optically bianisotropic NPs [31] can support the quasitrapped modes (QTM) or, by other words, the quasibound states in the continuum (qBICs) [32,33]. In general, the trapped modes or BICs are protected eigenmodes of ideal lossless optical systems that remain perfectly localized without radiation into free space [34], providing their infinite Q-factor resonances and perfect confinement of optical energy [35–37]. In practical cases, access to similar states can be obtained by weak distortion or perturbation of the ideal structure’s symmetrical properties that converts the trapped modes into QTM (qBICs) [38,39]. For metasurfaces, such perturbations can be realized by exploiting the bianisotropic properties of their building blocks.

Recently, it was analytically demonstrated in Ref. [40] that in the metasurfaces composed of dielectric nanodisks having a round penetrating hole shifted from the disk’s center, the QTM are generated by the self-synchronization for the individual disk’s magnetic dipole moments oriented orthogonally to the metasurface and excited due to the disk’s bianisotropic response. The strength of this effect depends on the values of the nondiagonal elements of the disk’s dipole polarizability tensor that is responsible for the bianisotropy [31,40]. In the case of the QTM excitation, the transmission and reflection spectra of arrays of such particles have the high-quality resonant features [39,40]. Moreover, the excitation of QTM leads to a strong near-field enhancement, which may initiate the nonlinear [41] and thermal [42] processes in the metasurfaces.

So far, the referenced results related to QTM concerned the metasurfaces composed of nanoparticles with isotropic dielectric properties. In these cases, only shape/size and aspect ratio factors can be applied to the realization of the required resonances of single particles. However, two-dimensional (2D) layered anisotropic materials [43] for building blocks can provide an additional degree of freedom for tuning and control of their optical resonances. This degree of freedom can provide a strong dependence of the optical response on the orientation of the field strength of the incident wave relative to the material layers even for scatterers of high-symmetrical shapes (such as spheres, cubes, and cylinders). Such materials include, in particular, the class of transition metal dichalcogenides (TMDCs) [44]. They can exist as layers with atomic thickness and flakes. In this form, they are promising for micro- and optoelectronics, photonics and are considered as the basis for creating a new type of transistors [45,46], biosensors [47] and spaser systems [48,49].

Bulk TMDCs, which consist of many parallel atomic monolayers weakly coupled to each other by van der Waals forces, show promising application potential in metasurfaces and metacoatings to control the polarization and angular characteristics of scattered light. One of these materials is MoS₂ [50–54], for which the real part of the refractive index along the layers is significantly higher than across the layers. If a bulk nanoparticle (disk, cone, and pyramid) is cut from a multilayer film of such material, then the layers will be parallel to the base. However, the experimental synthesizing of TMDCs with vertically aligned layers has been recently reported [55–57]. Therefore, in a metasurface composed of

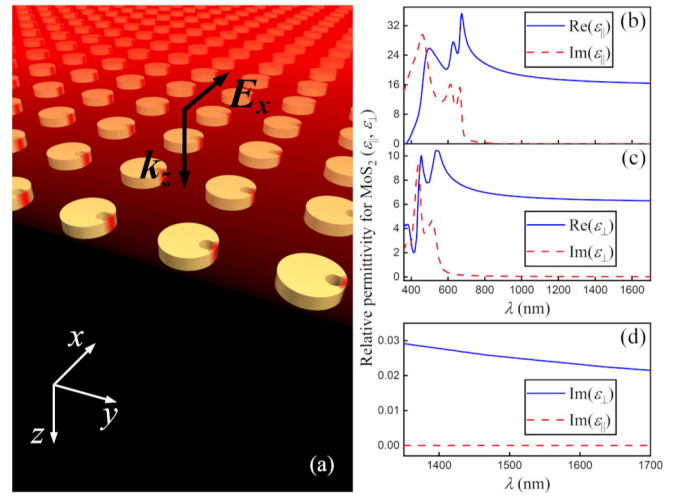


FIG. 1. (a) The model of metasurface composed of hollow MoS₂ disks with visualization of the electric field component in the regime of quasitrapped mode generation stylized on the base of numerical simulation. Relative dielectric permittivity for MoS₂ (b) along and (c) orthogonal to the material layers [50]. (d) The comparison of imaginary parts of permittivities for mutually orthogonal directions.

MoS₂ building blocks with vertically aligned layers, the effective refractive index for optical waves propagating along the metasurface is significantly higher than for an incident wave with polarization oriented perpendicular to the layers. This allows for realizing a spectrally solitary QTM of a metasurface and achieving high-contrast values, for example, for the reflectance R at the QTM wavelength relative to its vicinity. Therefore, an additional degree of freedom due to the difference in the refractive indices of an anisotropic material along two orthogonal directions determines one more way to control the spectral position of the QTM and its characteristics in the metasurface.

To clarify and demonstrate these new facilities, in this article we investigate the light scattering by individual MoS₂ disk particles and the realization of quasitrapped mode in the metasurfaces composed of such particles with vertically aligned layers. We show that, due to the QTM response of the metasurfaces, an effective narrow absorption band can be realized in the telecom (wavelength ~ 1550 nm) spectral range, where MoS₂ material has very weak anisotropic absorption. Finally, we investigate the possibilities of light polarization transformations caused by the MoS₂ disks metasurface by analogy with the effect of birefringence in anisotropic bulk media.

II. RESONANT EFFECTS IN MoS₂ METASURFACES

This article considers metasurfaces composed of disk nanoparticles made of MoS₂ with layers perpendicular to the disk base and parallel to the yz plane [Fig. 1(a)]. Every disk has radius R_2 , height H , and a through hole with radius R_1 . The hole can be shifted by Δ along the y axis (along the MoS₂ layers), as is shown in Fig. 1(a). The normal irradiation conditions are also shown in Fig. 1(a), where $E = (E_x, 0, 0)\exp(ikz)$ [$H = (H_y, 0, 0)\exp(ikz)$] are the

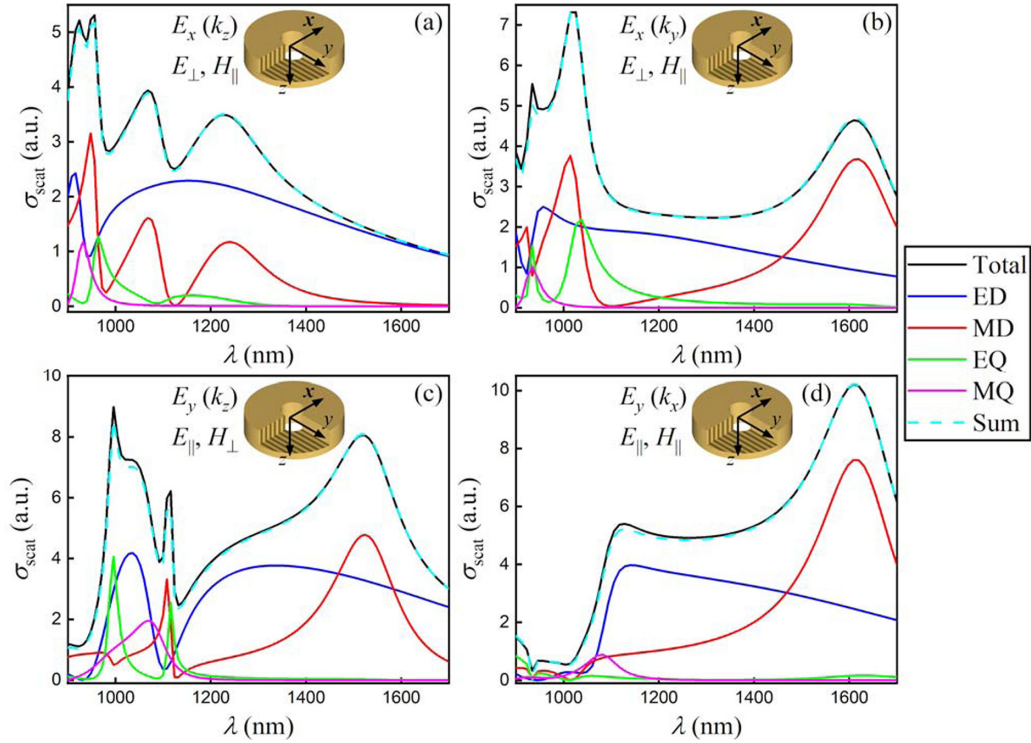


FIG. 2. Spectra of the scattering cross sections with corresponding multipole decomposition calculated for the MoS₂ disk (the radius and height $R_2 = H = 258$ nm) with the central through hole (the radius $R_1 = 82$ nm) and for different irradiation conditions clarified by the insets. Orientation of the MoS₂ layers is parallel to the yz plane.

incident electric and magnetic fields, \vec{k} is the wave vector of the normally incident plane wave.

A. Optical properties of single disks

Since the properties of metasurfaces are determined by the combinations of individual particles' resonances and the collective resonances of the total structure. We start from a detailed discussion, the question of how the anisotropy of MoS₂ dielectric permittivity [50] affects the scattering of light by the single MoS₂ disks with the symmetric through hole. In the Cartesian coordinate system shown in Fig. 1(a), the tensor of dielectric permittivity $\hat{\epsilon}_p$ is written as

$$\hat{\epsilon}_p = \begin{pmatrix} \epsilon_{\perp} & 0 & 0 \\ 0 & \epsilon_{\parallel} & 0 \\ 0 & 0 & \epsilon_{\parallel} \end{pmatrix}, \quad (1)$$

where the values of ϵ_{\perp} and ϵ_{\parallel} for MoS₂ (space group 194: $P6_3/mmc$) have been recently measured [50,53] and shown in Figs. 1(b) and 1(c). For calculations of the scattering cross sections and their corresponding multipole decompositions, we apply the following approach: the electric and magnetic fields, induced polarization, and density of the displacement current inside the scatterers are calculated using the COMSOL Multiphysics facilities for the problem of light plane wave scattering by a finite-size target, and then the contributions of the main multipole moments into the scattering cross

section σ_{scat} are determined from the expression [58]

$$\begin{aligned} \sigma_{\text{scat}} \simeq & \frac{k^4}{6\pi\epsilon_0^2|\mathbf{E}|^2} |\mathbf{p}|^2 + \frac{k^4\epsilon_d\mu_0}{6\pi\epsilon_0|\mathbf{E}|^2} |\mathbf{m}|^2 \\ & + \frac{k^6\epsilon_d}{720\pi\epsilon_0^2|\mathbf{E}|^2} \sum_{\alpha\beta} |Q_{\alpha\beta}|^2 + \frac{k^6\epsilon_d^2\mu_0}{80\pi\epsilon_0|\mathbf{E}|^2} \sum_{\alpha\beta} |M_{\alpha\beta}|^2 \\ & + \frac{k^8\epsilon_d^2}{1890\pi\epsilon_0^2|\mathbf{E}|^2} \sum_{\alpha\beta\gamma} |O_{\alpha\beta\gamma}|^2, \end{aligned} \quad (2)$$

where k is the vacuum wave number, ϵ_0 and ϵ_d are the vacuum dielectric and relative dielectric constants of surrounding medium, respectively, μ_0 is the vacuum permeability, \mathbf{E} is the vector of electric amplitude of the incident plane waves, \mathbf{p} and \mathbf{m} are the vectors of electric and magnetic dipole moments of the scatterer, respectively, and \hat{Q} , \hat{M} , and \hat{O} are the tensors of electric and magnetic quadrupole moments, and electric octupole moment, respectively. Corresponding expressions for the multipole moments defined by the density of the displacement current can be found elsewhere [58]. In this article we consider that all multipole moments of individual nanoparticles are located at their center of mass. This also concerns the calculation of the dipole polarizabilities presented further.

The scattering cross sections for different irradiation conditions are shown in Fig. 2. Independently on these conditions, the scattering in the telecom optical range ($\lambda \in [1250-1650]$ nm) is determined by the electric dipole (ED) and magnetic dipole (MD) moments of the disk. For the normal incidence of

the plane waves along the z axis [Figs. 2(a) and 2(c)], one can see the strong influence of the incident wave polarization on the spectral positions of ED and MD resonances caused by the MoS₂ dielectric anisotropy. Changing the electric polarization from E_x [being perpendicular to MoS₂ layers, Fig. 2(a)] to E_y [being parallel to MoS₂ layers, Fig. 2(c)], the value of the cross section increases, and the dipole resonances are shifted to the “red” side. For the E_y polarization (electric field is directed along the layers), the resonant MD contribution increases considerably. In this case, the main MD _{y} moment is directed perpendicular to the layers and determined by the ring displacement current induced in these layers characterized by a large refractive index $n \sim \sqrt{\varepsilon_{\parallel}}$. The redshift follows from the estimation of the wavelength $\lambda_{\text{res}}^{\text{MD}}$ corresponding to the MD resonance of a dielectric particle with dimension D and having refractive index n : $\lambda_{\text{res}}^{\text{MD}} \sim Dn$ —for fixed D , the resonant wavelength increases with n . Thus, the normally propagating light waves with E_x polarization (perpendicular to the layer) do not excite resonant response of the disks around $\lambda = 1500$ nm, in contrast to the case of the orthogonal E_y polarization.

For the side irradiation and H_z polarization, the results are presented in Figs. 2(b) and 2(d). One can see that the spectral position of the first MD resonance ($\lambda = 1620$ nm) almost does not depend on the orientation of the external electric field with respect to the MoS₂ layers. In contrast, the corresponding scattering cross sections’ values are different: once the electric field is parallel to the MoS₂ layers, the scattering cross section is larger owing to the larger value of the induced displacement current in xy plane. In this case, the value of the resonant MD at $\lambda = 1620$ nm is also larger than for other cases shown in Fig. 2(b). Due to the symmetry properties of the disk, the MD excited by the side irradiation with H_z polarization has the only m_z component for which

$$|m_z^{\parallel}| > |m_z^{\perp}|, \quad (3)$$

where $m_z^{\parallel(\perp)}$ is the MD z component for the side irradiation with electric field polarization parallel (perpendicular) to the MoS₂ layers. The inequality (3) is followed from the anisotropy of $\hat{\varepsilon}_p$, which also results in the nonlocal optical response of the MoS₂ disk.

In the dipole approximation with the inclusion of the first-order nonlocal response, the electric and magnetic dipole moments of single NPs irradiated by an external wave with electric \mathbf{E} and magnetic \mathbf{H} fields can be written in the form [59]

$$\mathbf{p} = \hat{\alpha}^{ee}\mathbf{E} + \hat{\alpha}^{em}\mathbf{H} + \hat{\alpha}[\nabla \otimes \mathbf{E}], \quad (4)$$

$$\mathbf{m} = \hat{\alpha}^{mm}\mathbf{H} + \hat{\alpha}^{me}\mathbf{E} + \hat{\alpha}[\nabla \otimes \mathbf{E}], \quad (5)$$

where $\hat{\alpha}^{ee(mm)}$ is the tensor of electric (magnetic) dipole polarizability corresponding to the direct (local) excitation of the dipole moment by the electric (magnetic) field of the incident wave. The second and third terms in (4) and (5) correspond to the bianisotropic and nonlocal, respectively, excitation of \mathbf{p} and \mathbf{m} . From the reciprocity property of the considered scattering systems, the tensors of bianisotropic polarizabilities satisfy the following relation: $\mu_0 \hat{\alpha}^{me} = -(\hat{\alpha}^{em})^T$ [60],

where T denotes the transpose operation. Moreover, from the deriving of (4) and (5) [61], the elements of the tensors $\hat{\alpha}$ and $\hat{\alpha}$ satisfy the following symmetry properties: $a_{ijl} = a_{ilj}$ and $c_{ijl} = c_{ilj}$. Furthermore, we will consider that when the orientation of the excited dipole is collinear with the wave vector of the incident wave, the bianisotropy is longitudinal, and when it is perpendicular, the bianisotropy is transverse. Note that all tensor coefficients in (4) and (5) depend only on geometrical and material characteristics of scatterers and are independent on irradiation conditions.

In order to determine the conditions of resonant coupling between NPs periodically arranged in a metasurface (as shown in Fig. 1), one needs to know certain components of the tensor coefficients from (4) and (5) which correspond to the lateral irradiation of the single disk [40,62]. They can be obtained from (4) and (5) if the dipole moments \mathbf{p} and \mathbf{m} of NP are known from numerical calculations for the two separate irradiation conditions (along x and y direction). For example, in the case of studying coupling effects with a magnetic dipole moment being perpendicular to the metasurface plane, it is convenient to get from (4) the system of equations in the form

$$m_z^{(k,E,H)} = \alpha_{zz}^{mm} H_z + c_{zyx} ik E_y + \alpha_{zy}^{me} E_y, \quad (6a)$$

$$m_z^{(-k,E,-H)} = -\alpha_{zz}^{mm} H_z - c_{zyx} ik E_y + \alpha_{zy}^{me} E_y, \quad (6b)$$

$$m_z^{(E,k,-H)} = -\alpha_{zz}^{mm} H_z + c_{zxy} ik E_x + \alpha_{zx}^{me} E_x, \quad (6c)$$

$$m_z^{(E,-k,H)} = \alpha_{zz}^{mm} H_z - c_{zxy} ik E_x + \alpha_{zx}^{me} E_x. \quad (6d)$$

Equations (6a) and (6b) correspond to the irradiation of NPs in two opposite directions: forward and backward to the x axis, while maintaining the direction of the vector \mathbf{E} along the y axis, see the coordinate system, for example, in the insets in Fig. 2. This information is indicated by the superscripts for m_z . Equations (6c) and (6d) correspond to the irradiation in forward and backward directions along the y axis while maintaining the direction of the vector \mathbf{E} along the x axis (see the corresponding superscripts for the moment). Using the symmetrical property $c_{zxy} = c_{zyx}$, the solution of system (6) in the general case have the form

$$\alpha_{zz}^{mm} = \frac{1}{4H_z} [(m_z^{(k,E,H)} - m_z^{(-k,E,-H)}) + (m_z^{(E,-k,H)} - m_z^{(E,k,-H)})], \quad (7a)$$

$$c_{zxy} = \frac{1}{2ik(E_x + E_y)} [(m_z^{(k,E,H)} - m_z^{(-k,E,-H)}) - (m_z^{(E,-k,H)} - m_z^{(E,k,-H)})]. \quad (7b)$$

Note that disks with a central hole have inverse symmetry. Therefore, there is no bianisotropy of any type in them, but a nonlocal response can be excited. The appearance of the nonlocal response is a consequence of the anisotropy of NP material, since for these irradiation conditions this effect is not observed in isotropic disks [63] for which the magnetic dipole component m_z is determined only by the local term with α_{zz}^{mm}

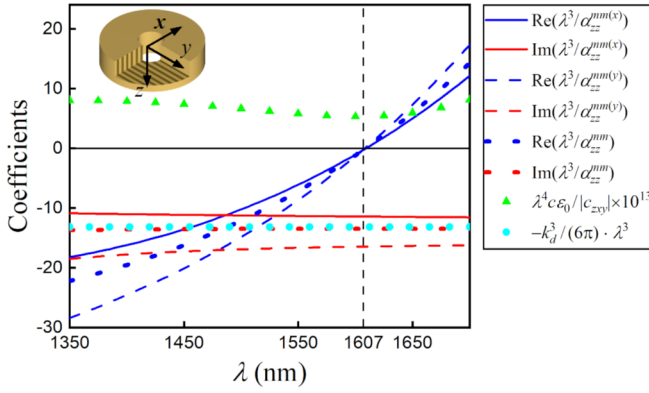


FIG. 3. Real (blue curves) and imaginary (red curves) parts of inverse polarizabilities and nonlocal response (green triangles) calculated according to (7) for α_{zz}^{mm} (dotted curves) and derived from (6a) and (6b) for the effective $\alpha_{zz}^{mm(x)}$ (solid curves) and $\alpha_{zz}^{mm(y)}$ (6c) and (6d) (dashed curves), separately, for lossless MoS₂ disk with radius and height $R_2 = H = 258$ nm with a centered hole with radius $R_1 = 82$ nm and vertically aligned layers shown in the inset. The cyan circles correspond to the analytical expression (11b) for the dipole sum.

in (6). Formally, we can also include the nonlocal response in effective polarizabilities (which become dependent on irradiation conditions), defining them as

$$\alpha_{zz}^{mm(x)} = \frac{m_z^{(k,E,H)}}{H_z} \quad \text{and} \quad \alpha_{zz}^{mm(y)} = \frac{m_z^{(E,-k,H)}}{H_z} \quad (8)$$

under the irradiation with a wave vector that is collinear to the x and y axes, respectively. Note that such effective polarizabilities of isotropic disks with a dipole response coincide with their direct polarizabilities α_{zz}^{mm} . The inverse values of the corresponding polarizabilities calculated for the disk NP with the central hole as in Fig. 2 are presented in Fig. 3 for different incident wavelengths λ . The curves corresponding to the direct (local) dipole polarizability α_{zz}^{mm} and its effective counterparts $\alpha_{zz}^{mm(x)}$ and $\alpha_{zz}^{mm(y)}$ significantly differ because of the nonlocal response additions. Note that the intersection point of the real parts of the inverse direct (local) and effective polarizabilities corresponds to their zero values coinciding with the magnetic-dipole resonant condition $\text{Re}(1/\alpha_{zz}^{mm}) = 0$ realized at the telecom wavelength $\lambda = 1607$ nm, see Fig. 3. At the same time, the imaginary parts of $1/\alpha_{zz}^{mm(x)}$ and $1/\alpha_{zz}^{mm(y)}$ do not coincide in all considered spectral ranges, including the resonant condition, which leads to the difference in the values of the dipoles $m_z^{(k,E,H)}$ and $m_z^{(-k,E,-H)}$ and, therefore, to different energies of their excitation.

In the region of small wavelengths around $\lambda = 950$ nm, multipeak dependence on the scattering cross section [Fig. 2] appears due to the anisotropic properties of the disk and quadrupoles excitation. However, in our further consideration, we shall concentrate our attention only on the telecom long-wavelength region, where the NP optical properties are determined only by their dipole response.

B. Quasitrapped modes of MoS₂ metasurfaces

According to (4) and (5) under $E = (E_x, 0, 0)\exp(ikz)$ irradiation conditions, the electric and magnetic dipole moments excited in a single disk NP can be determined as follows:

$$p_i = \alpha_{ix}^{ee} E_x + \alpha_{iy}^{em} H_y + a_{ixz} ik E_x, \quad (9a)$$

$$m_i = \alpha_{iy}^{mm} H_y + \alpha_{ix}^{me} E_x + c_{ixz} ik E_x. \quad (9b)$$

In the case of $i = z$, second terms correspond to the longitudinal bianisotropy, which can be used for excitation of the quasitrapped modes of the metasurface composed of such disks, as it has been discussed in Ref. [40]. The bianisotropic response of the single disk can appear due to the violation of its inverse symmetry, which is achieved, for example, by shifting a hole on a value Δ_y along the in-plane y axis of the Cartesian coordinate system, see inset in Fig. 4(a). In this case, the magnetic-type longitudinal bianisotropy leading to nonzero values of m_z , is associated with the term $\alpha_{zx}^{me} E_x$ in (9). Note that to obtain the longitudinal bianisotropy of the electric type leading to nonzero values of p_z , it is sufficient to change the polarization of the incident wave from E_x to E_y .

Spectral positions of multipole resonances of single dielectric disks can be tuned by variation of their geometrical parameters [64,65]. For the MoS₂ disks with holes shifted along MoS₂ layers with ε_{\parallel} (along the y axis) and normally irradiated by plane waves with electric field $E = (E_x, 0, 0)\exp(ikz)$, the results of such tuning procedure are shown in Fig. 4(a). This figure presents the contour plot of the scattering cross sections of MoS₂ disks with $H = R_2$, $R_1 = 0.318R_2$, and $\Delta_y = 0.38R_2$ over the parametric plane ($\lambda; R_2$). For the convenience of the result analysis, Fig. 4(a) also includes separate contributions of m_z into the total scattering cross sections excited due to the bianisotropic response with α_{zx}^{me} . One can see that with an increase of the disk radius and height, its resonances, including the resonant m_z contribution, shift to longer wavelengths. Note that the bianisotropic resonance m_z has a spectral position separated from the main resonances. The importance of this behavior will be seen from further consideration. Note that the redshift of m_z resonance is solely due to the orientation of the MoS₂ layers relative to the incident field. In particular, the wavelength λ_i of the main scattering resonances for a disk is proportional to its effective refractive index. Since the layers are arranged perpendicular to the exciting field E_x , this effective refractive index is mainly determined by the component ε_{\perp} . Therefore, $\lambda_i \approx n_{\perp} D$. However, the polarizability α_{zx}^{me} and the position of the resonance λ_{bi} for m_z are determined by the effective refractive index already depending on both parameters ε_{\parallel} and ε_{\perp} , i.e., $\bar{n} = f(\varepsilon_{\parallel}, \varepsilon_{\perp})$. Taking into account that $\varepsilon_{\parallel} > \varepsilon_{\perp}$, we obtain $\lambda_{bi} > \lambda_i$, which corresponds to the redshift of bianisotropic component. The main resonances are in the region of short wavelengths, see Fig. 4(a).

To have the bianisotropic m_z resonance in the middle of the telecom range, we choose the disks with $R_2 = 258$ nm and $H = 258$ nm for the formation of metasurfaces. The disks of such sizes have been studied in Sec. II A, where the dependence of their main optical resonances' spectral positions on the irradiation conditions was explained. The results obtained for such disks qualitatively correspond (excluding the bianisotropy) to the disks with a shifted hole because the

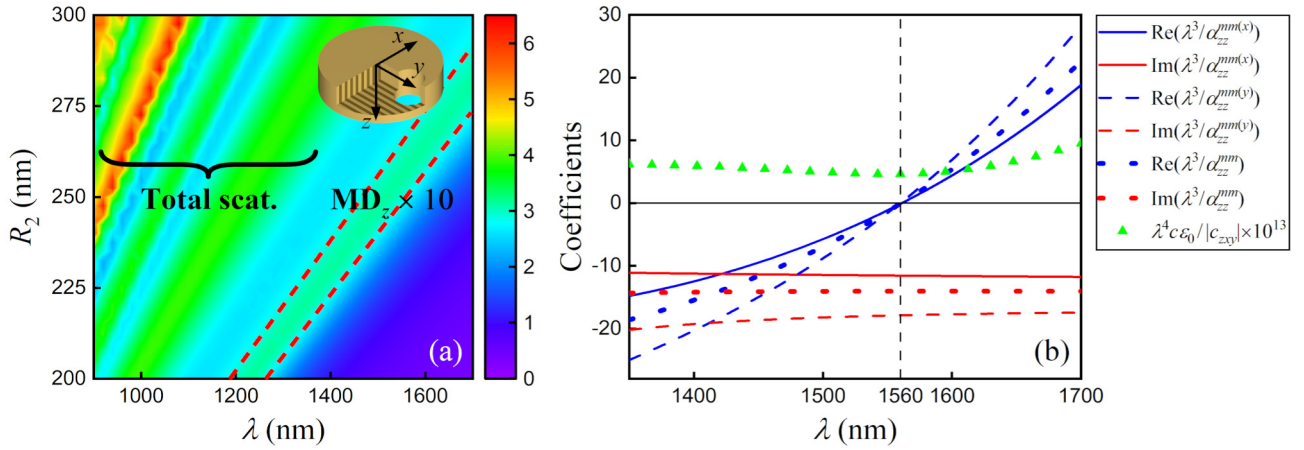


FIG. 4. (a) The contour plot on the parametric plane (λ ; R_2) for total scattering cross section (a.u.) and the partial scattering cross section associated only with MD component m_z (MD_z) calculated for MoS₂ disks with an eccentric hole normally irradiated by linear E_x -polarized waves. The hole with radius $R_1 = 0.318R_2$ is shifted on $\Delta_y = 0.38R_2$, inset in (a) shows the position of the shifted hole in a disk relative to the axes of the Cartesian coordinate system and schematic illustration of orientation of MoS₂ layers. The disk's height $H = R_2$. (b) The same as in Fig. 3, but for the disk with this shifted hole.

shift can be considered only as a weak perturbation. Note that the chosen proportions $R_1 = 0.318R_2$ and $\Delta_y = 0.38R_2$ were preliminarily obtained as a result of optimization for the observation of close to maximum values of MD_z in each disk with a fixed hole $R_2 = 258$ nm. It was found that a decrease in the hole size R_1 and/or Δ_y leads to a decrease in the contribution of the bianisotropic component m_z to the near-field response of each disk. This can decrease the visibility of BIC formed in a metasurface composed of such disks.

Before studying the optical properties of metasurfaces composed of the MoS₂ disks with the bianisotropic response, let us discuss some general positions related to the existence and excitation of BICs in metasurfaces composed of dipolar particles. As it has been discussed in Refs. [40,66], in the case of zero ohmic losses, the collective effect of synchronization of individual magnetic moments m_z in an infinite periodic array of holey isotropic disks (with the dipole response) placed in the xy plane with the period P can lead to the formation of BICs in the regime of the realization of trapped mode. If the magnetic dipole moment m_z is associated only with the direct dipole polarizability α_{zz}^{mm} , the condition for the formation of a trapped mode corresponds to the solution of the transcendental equation in the form [40,66]

$$S_z^{(R)} = \text{Re}\left(\frac{1}{\alpha_{zz}^{mm}}\right), \quad (10)$$

where $S_z^{(R)}$ is the real part of the dipole sum $S_z = S_z^{(R)} + iS_z^{(I)}$ with an infinite number of terms. The corresponding parts can be determined as follows:

$$S_z^{(R)} = \frac{k_d^2}{4\pi} \sum_{l,j} \left(\frac{\cos(k_d d_{lj})}{d_{lj}} - \frac{\sin(k_d d_{lj})}{k_d d_{lj}^2} - \frac{\cos(k_d d_{lj})}{k_d^2 d_{lj}^3} \right), \quad (11a)$$

$$S_z^{(I)} = -\frac{k_d^3}{6\pi}, \quad (11b)$$

where the last equality is obtained in the nondiffractive regime for which the period P of the array is smaller than the incident wavelength (so that $k_d P < 2\pi$) [2]. Here the parameter $d_{lj} = P\sqrt{l^2 + j^2}$ is the distance from the Cartesian coordinate system origin, coinciding with the position of a lattice node, to all other nodes of the lattice, which are numbering by indices l and j , $k_d = 2\pi/\lambda_d$, and λ_d is the incident wavelength in the surrounding medium with relative dielectric constant ϵ_d . In this paper we consider that $\epsilon_d = 1$.

Using (10) and (11a) together with α_{zz}^{mm} , it is possible to determine the lattice period P for a given wavelength of trapped mode λ_{TM} [62]. For example, we can fix the single particle polarizability α_{zz}^{mm} at a certain wavelength (λ_{TM}) and then, by solving (10), find the period P of a metasurface (with a square elementary cell) that will support the trapped mode state at this λ_{TM} . Note, since the imaginary part $S_z^{(I)}$ of the dipole sum in (11b) does not depend on the lattice period P , (11b) is always correct in the nondiffractive regime. Let us consider the equation

$$S_z^{(I)} = \text{Im}\left(\frac{1}{\alpha_{zz}^{mm}}\right), \quad (12)$$

providing together with (10) the second condition for the existence of a symmetry protected BIC or, in other words, a trapped mode with infinite quality factor. However, condition (12) can be exactly satisfied only in the case of the dipole response without ohmic losses, when $\text{Im}(1/\alpha_{zz}^{mm}) = -k_d^3/(6\pi)$ [40,66].

In general, the electric and magnetic dipole moments of NPs can include the contributions stemming from the nonlocality, including the bianisotropy, see (4) and (5). In these cases, the metasurfaces composed of such dipole NPs cannot support the ideal BICs. However, in this case, the so-called qBIC or QTM can be realized. It is characterized by finite quality factors, the values of which are determined by the bianisotropic contributions. However, as shown in our calculations, even in the cases of the nonlocality, the relation (10)

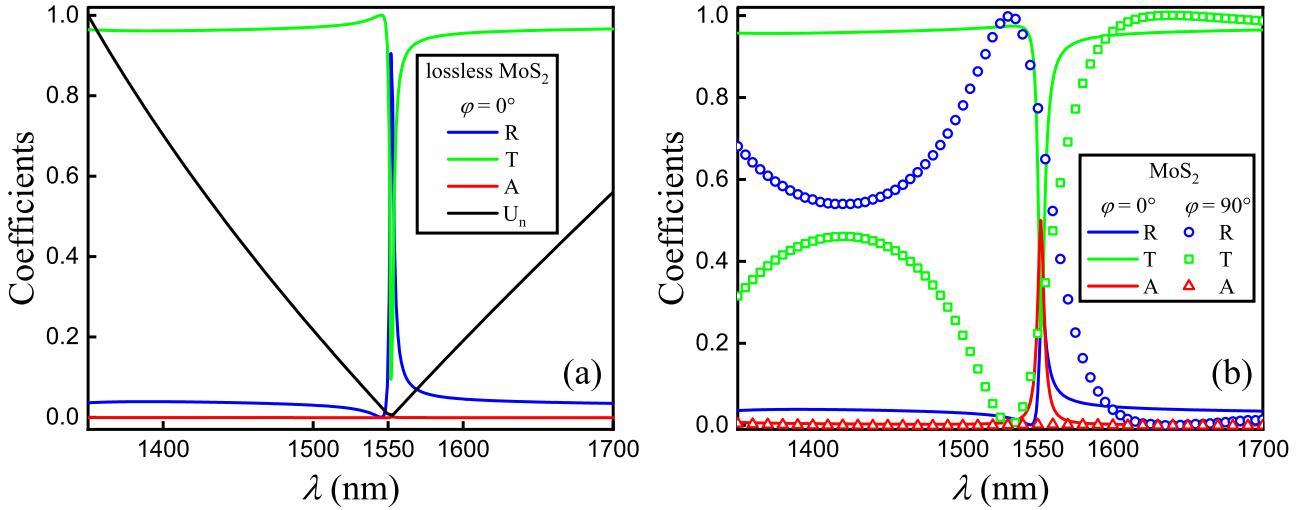


FIG. 5. Spectra of the reflection (R), transmission (T), absorption (A) coefficients and parameter U_n for array with period $P = 1063$ nm composed of (a) ideal lossless and (b) real weakly absorbing MoS_2 disks; $U_n = U/\max(U)$, where $U = |\mathcal{S}_z^{(R)} - \text{Re}(1/\alpha_{zz}^{mm})|$; the condition $U_n = 0$ indicates the position of QTM. The geometric disk parameters correspond to Fig. 4(b). The angle φ determines the electric polarization of the incident waves: $\varphi = 0^\circ$ ($\varphi = 90^\circ$) determines the E_x (E_y) polarization.

only with α_{zz}^{mm} can be used to determine the lattice period P of the metasurface supporting a QTM at λ_{TM} . We assume that this follows from the fact that only dipole-dipole interaction is involved in the QTM formation, while a nonlocal response can be related to the generation of scatterer dipole moments by high order multipole parts of the incident wave [59].

Now, to approximately estimate the spectral position of a QTM, we examine a lossless MoS_2 disk with an eccentric hole, i.e., with the imaginary parts $\varepsilon_{\perp}^{(l)} = \varepsilon_{\parallel}^{(l)} = 0$ and with the bianisotropic response. As it was discussed above, we chose $H = R_2$, $R_2 = 258$ nm, $R_1 = 82$ nm, $\Delta_y = 98$ nm and calculate the polarizabilities α_{zz}^{mm} , and $\alpha_{zz}^{mm(x)}$, $\alpha_{zz}^{mm(y)}$ of the disk according to (7a). The forms of the curves for the real and imaginary parts of $1/\alpha_{zz}^{mm}$, $1/\alpha_{zz}^{mm(x)}$, and $1/\alpha_{zz}^{mm(y)}$ shown in Fig. 4(b) remain qualitatively the same as in Fig. 3. However, due to the bianisotropy induced by the hole shift, the resonance condition $\text{Re}(1/\alpha_{zz}^{mm}) = 0$ is realized at new wavelength $\lambda \approx 1562$ nm [Fig. 4(b)]. Note that $\text{Re}(1/\alpha_{zz}^{mm(x)}) = 0$ and $\text{Re}(1/\alpha_{zz}^{mm(y)}) = 0$ are also realized at this wavelength.

Thus, the considered anisotropic disk with an eccentric hole demonstrates the bianisotropic response in the IR range. It can be used as a building block for the creation of a metasurface supporting a QTM in a given spectral range. Choosing the wavelength $\lambda_{\text{QTM}} = 1552$ nm, at which a QTM is assumed to be realized, and taking $\text{Re}(1/\alpha_{zz}^{mm})$ at this wavelength [Fig. 4(b)], we obtain from the solution of (10) the period $P = 1063$ nm of the metasurface. Note that the chosen combination of the wavelength of the incident wave and the cylinder's size corresponds to the region of strong bianisotropic response m_z in Fig. 4(a). This situation should guarantee a finite width of the QTM resonance because, in this case, $\text{Im}(\mathcal{S}_z) > \text{Im}(1/\alpha_{zz}^{mm})$.

To verify the dipole approximation, we numerically calculated, using COMSOL Multiphysics, the transmission and reflection spectra of the metasurface [Fig. 1(a)] composed of the hollow disks with the size parameters as in Fig. 4 and with

the period $P \approx 1063$ nm. As it is demonstrated in Fig. 5(a) for the lossless case, the transmission and reflection spectra have narrow resonant features just at the wavelength 1552 nm of the QTM. As it is followed from the dipole approximation [40], at this spectral region, the strong resonant m_z component of every disk is excited due to the realization of the QTM conditions. Simultaneously, owing to bianisotropy, there is also a coupling between m_z and p_x [40], so that the electric dipole component p_x of every disk is also resonantly increased, resulting in suppression of the transmission and increasing the efficiency of reflection. Thus this behavior is fully agreed with considerations provided by the dipole approximation. Note that the resonant values of m_z under QTM conditions lead to an increase in the near field in the metasurface plane since disks do not emit electromagnetic waves perpendicular to this plane [40]. Note that for the disks with a reduced value of the ratio $R_1 = 0.318R_2$ and/or shift $\Delta_y = 0.38R_2$ we observe a decrease in the value of MDz relative to the results of optimization in Fig. 4(a). Since the value of MDz determines the rate of energy pumping into the QTM from an external wave, a decrease in MDz leads to an increase in the quality factor of the QTM. This entails additional restrictions on the visibility of the effect since the fluctuations of the system parameters can destroy such an ultranarrow QTM resonance.

Furthermore, we will take into account that MoS_2 has small but finite values of the imaginary parts of its dielectric permittivities in the telecommunication range [Fig. 1(d)]. As a result, the absorption effect has to be realized in the metasurface with parameters as in Fig. 5(a) and with actual MoS_2 dielectric permittivity. Results of the transmission, reflection, and absorption spectra simulations for the two different polarization of the incident waves are shown in Fig. 5(b). Note that for the E_x polarization, the joint occurrence of dissipative effects in each building block and the collective effects of the QTM formation in the entire metasurface leads to the appearance of a narrow peak of collective losses at the wavelength of the QTM, see Fig. 5(b). This is due to the considerable

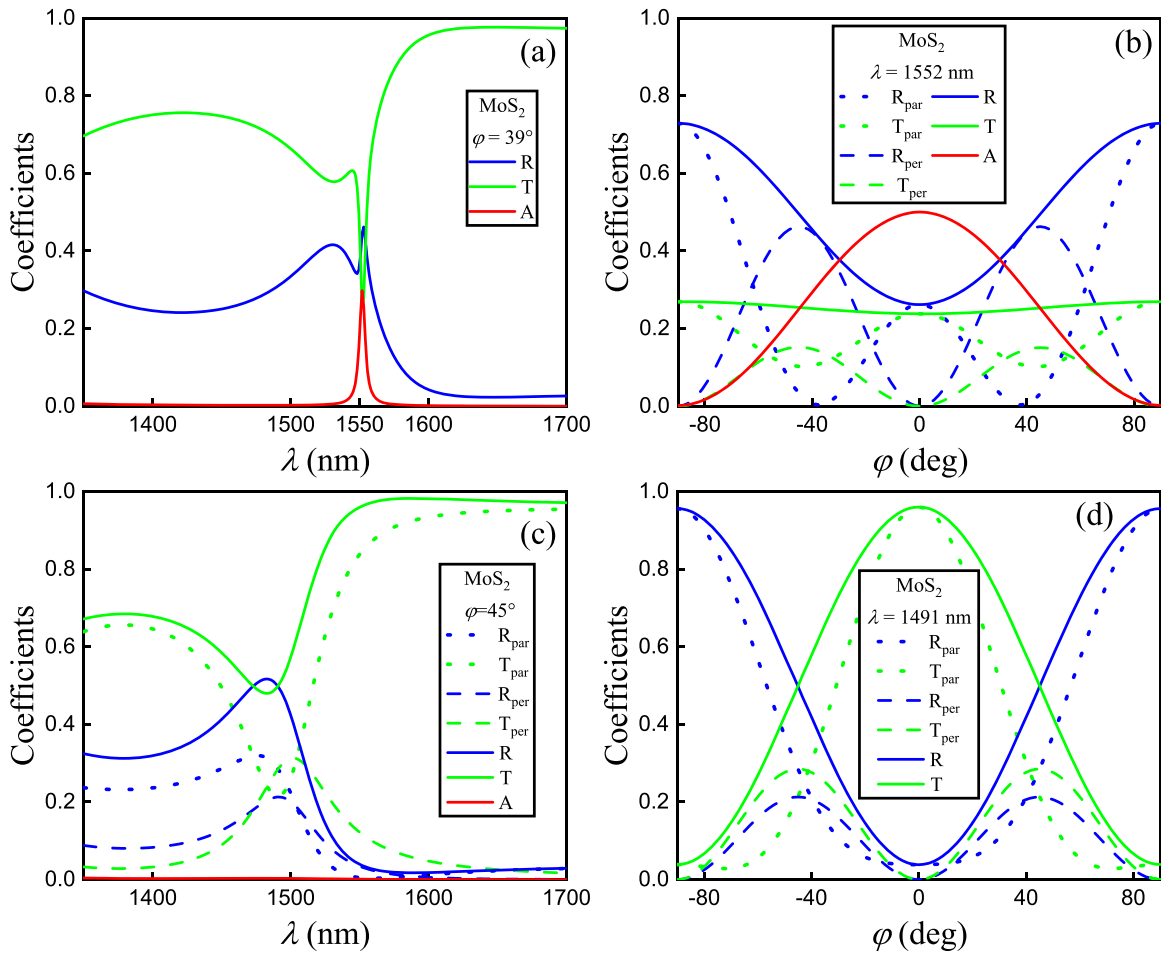


FIG. 6. Spectral and angular dependencies for the total reflection (R), transmission (T), and absorption (A) coefficients and their collinear (R_{par} , T_{par}) and orthogonal (R_{per} , T_{per}) polarization components of the reflected and transmitted waves for an array with period $P = 1063$ nm of absorbing MoS_2 disks with (a) and (b) shifted hole and parameters corresponding to Fig. 4(b) and with (c) and (d) centered hole and parameters corresponding to Fig. 3. The angle φ determines the orientation of the electric polarization of the incident waves with respect to the x axis.

concentration of the electric field inside the cylinders under the QTM conditions. Indeed, the coupling between individual cylinders in the array occurs due to the interaction of their magnetic fields. They are significantly enhanced in the holes and induce the electric field hot spots inside the cylinders, which are the centers of collective absorption, see Fig. 7. This allows us to use such a dissipative metasurface for ultranarrowband absorbing in IR range or for highly sensitive detection of nano-objects near it.

Analyzing the absorption properties of the system, we found that under the selected conditions in Fig. 5(b), the absorption efficiency is high and equals to 51% at $\lambda_{\text{QTM}} = 1552$ nm. The quality factor $Q = \lambda/\text{FWHM}$ is 310 for the FWHM of absorption peak equals only to 5 nm. In addition, the system demonstrates a high $S = 380$ nm/RIU (refractive index unit) sensitivity to the environment and reaches the level of a figure of merit (FOM) $\text{FOM} = 76$. This corresponds to a good level of sensing, compare with Refs. [5,6,20,23]. Here we used the relations $S = \Delta\lambda/\Delta n$ and $\text{FOM} = S/\text{FWHM}$, where $\Delta\lambda$ is the wavelength shift of reflectance resonance as result of the environment refractive index Δn variation.

Another feature of the metasurface composed of the bianisotropic MoS_2 disks is a high polarization sensitivity. When

the electric field polarization of the incident wave is rotated in the xy plane by an angle $\varphi = \pm 90^\circ$ the QTM, including the collective dissipative effect, completely disappears after the vanishing of the longitudinal bianisotropy of the magnetic type, see the transmission, reflection, and absorption spectra in Fig. 5(b) calculated for $\varphi = 90^\circ$. Here φ is the rotation angle in the xy plane of the electric polarization relative to the x axis: $\varphi = 0^\circ$ ($\varphi = 90^\circ$) corresponds to the E_x (E_y) polarization.

In addition, we investigated the polarization sensitivity over the entire range of angles φ at the wavelength $\lambda_{\text{QTM}} = 1552$ nm and found the decreasing of the absorption maximum associated with the QTM with changing the angle φ from 0° to $\pm 90^\circ$. For the case $\varphi = 39^\circ$ the result is shown in Fig. 6(a). Note that the spectral position of the absorption maximum does not depend on the angle φ always remaining at the wavelength $\lambda_{\text{QTM}} = 1552$ nm. The dependence of the transmission, reflection, and absorption coefficients on the angle φ at this wavelength is shown in Fig. 6(b). From this figure we observe another feature: the rotation of the polarization of the normally incident wave initiates the process of transferring part of its energy into the components of the transmitted and reflected waves, which are orthogonal to the polarization

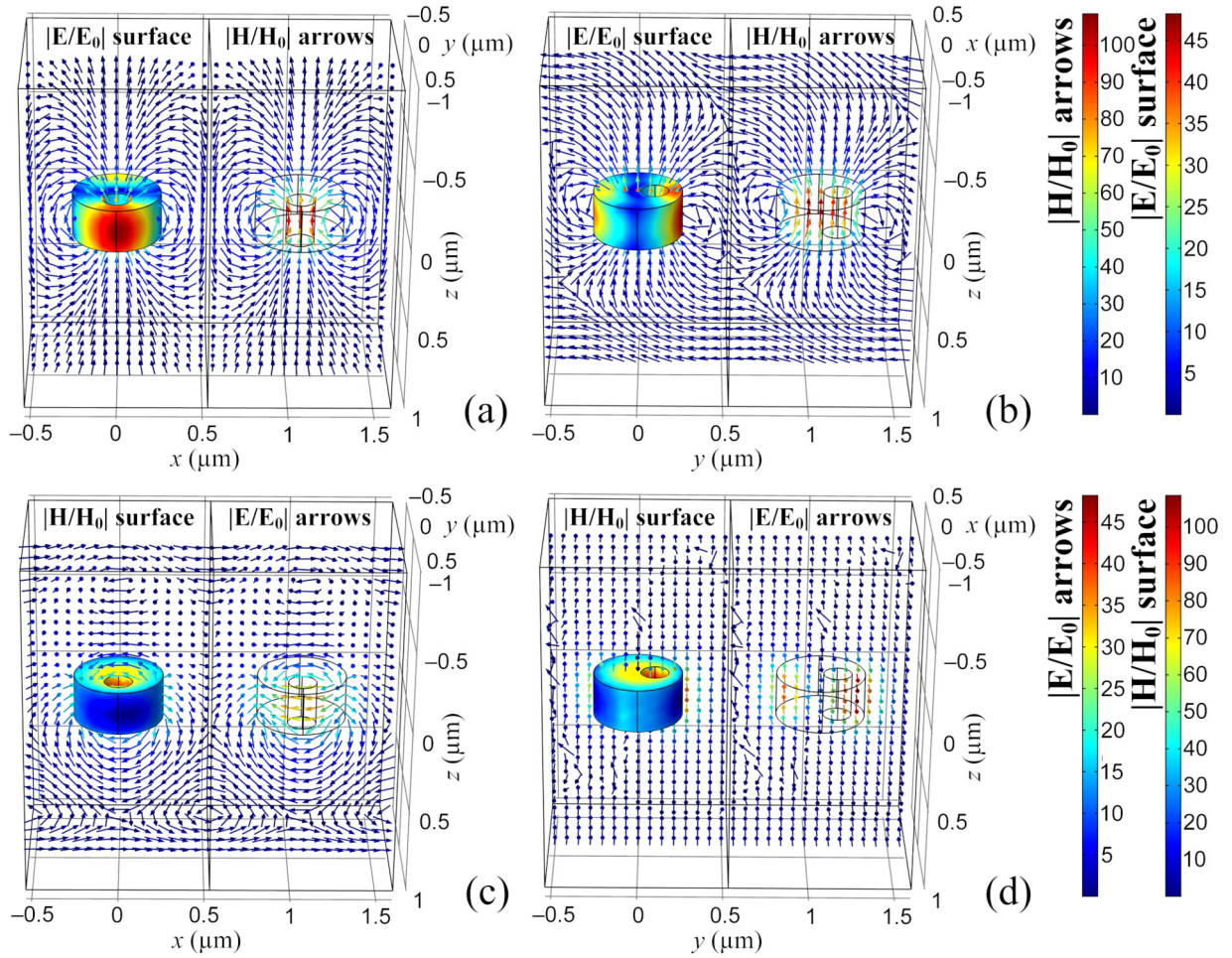


FIG. 7. The visualization of electric and magnetic field distributions calculated (a) and (c) in the xz plane and (b) and (d) in the yz plane for a pair of MoS₂ disks in the metasurface at the conditions of the QTM. The metasurface parameters correspond to Fig. 5(a).

of the incident wave. In particular, choosing the angle $\varphi = 39^\circ$ leads to the generation of the reflected wave only with linear polarization that is orthogonal to the polarization of the incident wave, see curve R_{per} in Fig. 6(b). The maximum of the energy transformation into the orthogonal component of the transmitted and reflected waves is realized at the angle $\varphi = 45^\circ$ for both parameters R_{per} and T_{per} [Fig. 6(b)]. Finally, we investigate the possibilities of light polarization transformations caused by the MoS₂ disks metasurface by analogy with the effect of birefringence in anisotropic bulk media.

In order to exclude any influence of the particle bianisotropy on the cross-polarization effect in the transmission and reflection, we analyzed this effect for the metasurface composed of disks with centered holes and also found its presence in the system, see Figs. 6(c) and 6(d). However, in this case, the maximum for R_{per} is realized at the wavelength of 1491 nm [see Fig. 6(c)]. Figure 6(d), plotted for this wavelength, demonstrates the conservation of the angular position of the maximum for R_{per} (T_{per}) at $\varphi = 45^\circ$. Our simulations of the metasurfaces, composed of the disks with similar geometry fabricated from isotropic material, showed that such metasurfaces do not possess the property of polarization transformation. Thus, we can conclude that the observed effects are associated with the anisotropic properties of individual build-

ing blocks. Hence, metasurfaces of subwavelength thickness composed of individual in-plane symmetric building blocks of anisotropic materials can have properties of a solid plate consisting of birefringent material. Note that in the opposite case with the use of the exciting wave $E_y(k_z)$ for the disks with a hole shifted along the x axis, the spectral position of the main resonances is determined by the value ε_{\parallel} , which shifts them to the infrared region. This leads to a spectral superposition of the resonances of the single disk and the QTM resonance, resulting in a decrease in the contrast of the QTM resonance. Such a case is poorly suited for the design of sensors and narrowband absorbers.

In the final part of this section we note another important feature of the quasitrapped modes in the metasurface of anisotropic NPs. This is the presence of the preferred direction of the interaction between them. Figure 7 shows the distribution patterns of the electric [by the color map on the cylinder surface in Figs. 7(a) and 7(b)] and magnetic [by the vectors in the chosen plane in Figs. 7(c) and 7(d)] and magnetic [by the vectors in the chosen plane in Figs. 7(a) and 7(b)] and by the color map on the cylinder surface in Figs. 7(c) and 7(d)] fields for the disks in the metasurface plotted for different views. It can be seen that strong near-field interactions between the individual disks are realized by connecting the magnetic field lines in

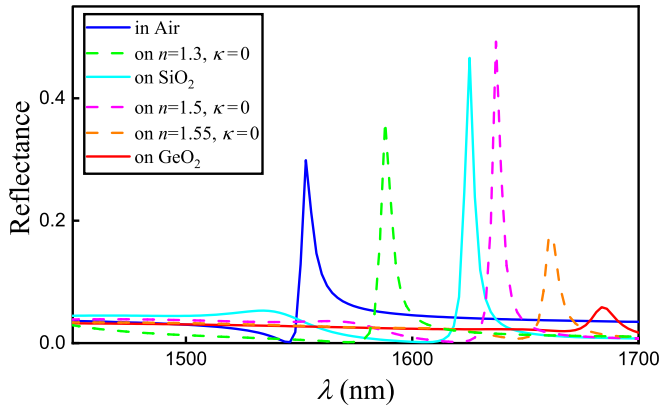


FIG. 8. Reflectance spectra for the metasurface (with period $P = 1063$ nm composed of MoS_2 disks with holes) placed in air (solid blue curve) and on semi-infinite substrates corresponding to quartz glass (solid cyan curve) [68], germanium dioxide (solid red curve) [69], and also artificial media with zero imaginary part of refractive index $\kappa = 0$ and different values for real part of refractive index $n = 1.3$ (dashed green curve), $n = 1.5$ (dashed magenta curve), and $n = 1.55$ (dashed orange curve). The parameters of disk correspond to Fig. 4.

the xz plane, see Fig. 7(a). At the same time, the magnetic field is tightened and concentrated in the holes of the disks with the formation of hot spots of the electric field in the narrow waist near them. On the contrary, the visualization of the magnetic field in the yz plane demonstrates the repulsion of the field strength lines [see Fig. 7(b)]. A similar picture is observed for the electric field vectors in the space between the cylinders in Figs. 7(c) and 7(d). We changed the polarization of the incident wave to $E_y(k_z)$ and shifted the hole along the x axis and found that an asymmetric field distribution, as in Fig. 7, does not depend on the method of the QTM excitation. Thus, the topology of the field for QTM is determined by the orientation of the layers of the anisotropic material used to fabricate the metasurface. In particular, the same character of the coupling is kept in the case of shifting the hole along the x axis and using the field $E = (0, E_y, 0)\exp(ikz)$ for irradiation of an array of disks with holes.

III. THE INFLUENCE OF THE SUBSTRATE ON THE QTM EXCITATION

The influence of a semi-infinite substrate on the realization of quasitrapped modes depends significantly on the refractive index n_{sub} of the substrate material. It can be seen from the results in Fig. 8 that increasing the refractive index of the substrate, first, leads to the redshift for the QTM resonance with an increase in the reflection maximum (the first regime). Second, starting from a certain value of the refractive index of the substrate, the reflection maximum gradually disappears (the second regime). The main factor limiting the visibility of the QTM effect is the grating diffraction into the substrate. Diffraction into the substrate occurs for waves with a wavelength of $\lambda \lesssim \lambda_D = n_{\text{sub}}P$. If the QTM is excited at the wavelength $\lambda_{\text{QTM}} > \lambda_D$ we have realization of the first regime, the cases $\lambda_{\text{QTM}} \lesssim \lambda_D$ correspond to the second regime, where the diffraction into the substrate appears. In our case the

first subdiffraction regime is satisfied for low-refractive index substrates with $n_{\text{sub}} < 1.55$. We note a nonmonotonic dependence of the shift of wavelength λ_{QTM} on n_{sub} . This could be related to the features of the substrate-induced additional magnetoelectric (bianisotropic) response of every metasurface's building blocks [67].

As a result, the possibility of direct observation of QTM in the presented MoS_2 metasurface with vertically aligned layers for building blocks placed on the SiO_2 substrate is confirmed by numerical calculations and described in corresponding discussion. The choice of another combination of the mechanism of QTM excitation, another material of building blocks and substrate, requires an additional optimization within the framework of the presented general strategy.

IV. CONCLUSION

In the present work we have studied the features of the optical response of disk NPs fabricated from an optically anisotropic material MoS_2 . The scattering cross sections for different irradiation directions have been calculated. It has been shown that spectral positions of multipole resonances are determined by not only the shape and size of the scatterer but also by the internal material anisotropy, which can affect the nonlocal optical properties of the scatterers. We have investigated the features of transmission and reflection spectra of metasurfaces composed of such nanoparticles and determined conditions for the excitation of QTM, leading to the formation of a narrow absorption band in the telecom spectral range. A cross-polarization effect was also found for the transmitted and reflected waves, and its spectral and angular features were studied. The critical role of material anisotropy in these transformations has been demonstrated. The obtained results can be used to design metasurfaces composed of weakly absorbing blocks and intended for narrow-band quenching of IR signals and fabrication of polarization-sensitive distributed sensors and polarization metacoatings. Along with direct physical-chemical approaches [70] to the creation of materials with special properties, the expansion of the material base for the implementation of metamaterials and metasurfaces opens up new possibilities for the development of optical devices for nanophotonic applications.

Note that for fabricating metasurfaces from two-dimensional materials, one can use electron beam lithography [71] in the case when building blocks have complex geometry as in this work. However, the possibility of observing the presented effects in metasurfaces based on spherical/elliptical nanoparticles with defects or dimers [72] fabricated by laser printing methods with the control of the phase composition [73] from two-dimensional materials is of considerable interest.

ACKNOWLEDGMENTS

This work was partially supported by the Russian Science Foundation, Grant No. 20-12-00343. Development of numerical algorithms was supported by the Ministry of Science and Higher Education of the Russian Federation (Agreement No. 075-15-2021-606).

- [1] J. B. Pendry, A. J. Holden, W. J. Stewart, and I. Youngs, *Phys. Rev. Lett.* **76**, 4773 (1996).
- [2] F. J. García De Abajo, *Rev. Mod. Phys.* **79**, 1267 (2007).
- [3] S. Zou, N. Janel, and G. C. Schatz, *J. Chem. Phys.* **120**, 10871 (2004).
- [4] X. Liu, K. Fan, I. V. Shadrivov, and W. J. Padilla, *Opt. Express* **25**, 191 (2017).
- [5] Y. Shen, J. Zhou, T. Liu, Y. Tao, R. Jiang, M. Liu, G. Xiao, J. Zhu, Z.-K. Zhou, X. Wang, C. Jin, and J. Wang, *Nat. Commun.* **4**, 2381 (2013).
- [6] D. Wu, R. Li, Y. Liu, Z. Yu, L. Yu, L. Chen, C. Liu, R. Ma, and H. Ye, *Nanoscale Res. Lett.* **12**, 427 (2017).
- [7] S. A. Kuznetsov, A. G. Paulish, A. V. Gelfand, P. A. Lazorskiy, and V. N. Fedorinin, *Appl. Phys. Lett.* **99**, 023501 (2011).
- [8] D. Yan, M. Meng, J. Li, and X. Li, *Front. Phys.* **8**, 306 (2020).
- [9] J. Wu, *Opt. Commun.* **435**, 25 (2019).
- [10] Y. V. Stebunov, O. A. Aftenieva, A. V. Arsenin, and V. S. Volkov, *ACS Appl. Mater. Interfaces* **7**, 21727 (2015).
- [11] L. Shi, J. Shang, Z. Liu, Y. Li, G. Fu, X. Liu, P. Pan, H. Luo, and G. Liu, *Nanotechnology* **31**, 465501 (2020).
- [12] D. Wu, Y. Liu, R. Li, L. Chen, R. Ma, C. Liu, and H. Ye, *Nanoscale Res. Lett.* **11**, 483 (2016).
- [13] X. Lu, R. Wan, and T. Zhang, *Opt. Express* **23**, 29842 (2015).
- [14] A. B. Evlyukhin, C. Reinhardt, A. Seidel, B. S. Luk'yanchuk, and B. N. Chichkov, *Phys. Rev. B* **82**, 045404 (2010).
- [15] P. Offermans, M. C. Schaafsma, S. R. K. Rodriguez, Y. Zhang, M. Crego-Calama, S. H. Brongersma, and J. Gómez Rivas, *ACS Nano* **5**, 5151 (2011).
- [16] A. B. Evlyukhin, C. Reinhardt, U. Zywiets, and B. N. Chichkov, *Phys. Rev. B* **85**, 245411 (2012).
- [17] V. E. Babicheva and A. B. Evlyukhin, *Laser Photonics Rev.* **11**, 1700132 (2017).
- [18] V. G. Kravets, A. V. Kabashin, W. L. Barnes, and A. N. Grigorenko, *Chem. Rev.* **118**, 5912 (2018).
- [19] C. Cherqui, M. R. Bourgeois, D. Wang, and G. C. Schatz, *Acc. Chem. Res.* **52**, 2548 (2019).
- [20] K. Fan, J. Y. Suen, X. Liu, and W. J. Padilla, *Optica* **4**, 601 (2017).
- [21] C.-Y. Yang, J.-H. Yang, Z.-Y. Yang, Z.-X. Zhou, M.-G. Sun, V. E. Babicheva, and K.-P. Chen, *ACS Photonics* **5**, 2596 (2018).
- [22] Y. Wang, D. Zhu, Z. Cui, L. Hou, L. Lin, F. Qu, X. Liu, and P. Nie, *ACS Omega* **4**, 18645 (2019).
- [23] Y. Wang, L. Yue, Z. Cui, X. Zhang, X. Zhang, Y. Q. Zhu, and K. Zhang, *AIP Adv.* **10**, 045039 (2020).
- [24] J. Tian, H. Luo, Q. Li, X. Pei, K. Du, and M. Qiu, *Laser Photonics Rev.* **12**, 1800076 (2018).
- [25] M. Y. Gubin, A. V. Shesterikov, A. V. Prokhorov, and V. S. Volkov, *Laser Photonics Rev.* **14**, 2000237 (2020).
- [26] J. Zhang, K. F. MacDonald, and N. I. Zheludev, *Opt. Express* **21**, 26721 (2013).
- [27] V. R. Tuz, V. V. Khardikov, and Y. S. Kivshar, *ACS Photonics* **5**, 1871 (2018).
- [28] M. Odit, P. Kapitanova, P. Belov, R. Alaee, C. Rockstuhl, and Y. S. Kivshar, *Appl. Phys. Lett.* **108**, 221903 (2016).
- [29] D. Pidgayko, I. Sinev, D. Permyakov, S. Sychev, F. Heyroth, V. Rutckaia, J. Schilling, A. Lavrinenko, A. Bogdanov, and A. Samusev, *ACS Photonics* **6**, 510 (2019).
- [30] E. Evlyukhin, S. A. Howard, H. Paik, G. J. Paez, D. J. Gosztola, C. N. Singh, D. G. Schlom, W.-C. Lee, and L. F. J. Piper, *Nanoscale* **12**, 18857 (2020).
- [31] T. G. Mackay and A. Lakhtakia, *Electromagnetic Anisotropy and Bianisotropy: A Field Guide* (World Scientific, Singapore, 2010).
- [32] K. Koshelev, A. Bogdanov, and Y. Kivshar, *Sci. Bull.* **64**, 836 (2019).
- [33] D. Khmelevskaia, D. I. Markina, V. V. Fedorov, G. A. Ermolaev, A. V. Arsenin, V. S. Volkov, A. S. Goltaev, Y. M. Zadiranov, I. A. Tzibizov, A. P. Pushkarev, A. K. Samusev, A. A. Shcherbakov, P. A. Belov, I. S. Mukhin, and S. V. Makarov, *Appl. Phys. Lett.* **118**, 201101 (2021).
- [34] F. Monticone, D. Sounas, A. Krasnok, and A. Alù, *ACS Photonics* **6**, 3108 (2019).
- [35] D. R. Abujetas, N. van Hoof, S. ter Huurne, J. G. Rivas, and J. A. Sánchez-Gil, *Optica* **6**, 996 (2019).
- [36] S. Li, C. Zhou, T. Liu, and S. Xiao, *Phys. Rev. A* **100**, 063803 (2019).
- [37] S. Han, P. Pitchappa, W. Wang, Y. K. Srivastava, M. V. Rybin, and R. Singh, *Adv. Opt. Mater.* **9**, 2002001 (2021).
- [38] V. A. Fedotov, M. Rose, S. L. Prosvirnin, N. Papasimakis, and N. I. Zheludev, *Phys. Rev. Lett.* **99**, 147401 (2007).
- [39] V. R. Tuz, V. V. Khardikov, A. S. Kupriianov, K. L. Domina, S. Xu, H. Wang, and H.-B. Sun, *Opt. Express* **26**, 2905 (2018).
- [40] A. B. Evlyukhin, V. R. Tuz, V. S. Volkov, and B. N. Chichkov, *Phys. Rev. B* **101**, 205415 (2020).
- [41] L. Xu, K. Z. Kamali, L. Huang, M. Rahmani, A. Smirnov, R. Camacho-Morales, Y. Ma, G. Zhang, M. Woolley, D. Neshev, and A. E. Miroshnichenko, *Adv. Sci.* **6**, 1802119 (2019).
- [42] K. Z. Kamali, L. Xu, J. Ward, K. Wang, G. Li, A. E. Miroshnichenko, D. Neshev, and M. Rahmani, *Small* **15**, 1805142 (2019).
- [43] K. S. Novoselov, A. Mishchenko, A. Carvalho, and A. H. C. Neto, *Science* **353**, aac9439 (2016).
- [44] J. Gusakova, X. Wang, L. L. Shiau, A. Krivosheeva, V. Shaposhnikov, V. Borisenko, V. Gusakov, and B. K. Tay, *Phys. Status Solidi A* **214**, 1700218 (2017).
- [45] B. Chakraborty, A. Bera, D. V. S. Muthu, S. Bhowmick, U. V. Waghmare, and A. K. Sood, *Phys. Rev. B* **85**, 161403(R) (2012).
- [46] M. Yu. Gubin, A. Yu. Leksin, A. V. Shesterikov, V. S. Volkov, and A. V. Prokhorov, *Appl. Surf. Sci.* **506**, 144814 (2020).
- [47] D. Sarkar, W. Liu, X. Xie, A. C. Anselmo, S. Mitragotri, and K. Banerjee, *ACS Nano* **8**, 3992 (2014).
- [48] C. Jayasekara, M. Premaratne, S. D. Gunapala, and M. I. Stockman, *J. Appl. Phys.* **119**, 133101 (2016).
- [49] M. Yu. Gubin, A. V. Shesterikov, S. N. Karpov, and A. V. Prokhorov, *Phys. Rev. B* **97**, 085431 (2018).
- [50] G. A. Ermolaev, D. V. Grudinin, Y. V. Stebunov, K. V. Voronin, V. G. Kravets, J. Duan, A. B. Mazitov, G. I. Tselikov, A. Bylinkin, D. I. Yakubovsky, S. M. Novikov, D. G. Baranov, A. Y. Nikitin, I. A. Kruglov, T. Shegai, P. Alonso-González, A. N. Grigorenko, A. V. Arsenin, K. S. Novoselov, and V. S. Volkov, *Nat. Commun.* **12**, 854 (2021).
- [51] M. Chhowalla, H. S. Shin, G. Eda, L.-J. Li, K. P. Loh, and H. Zhang, *Nat. Chem.* **5**, 263 (2013).
- [52] B. Schönfeld, J. Huang, and S. Moss, *Acta Crystallogr. Sect. B* **39**, 404 (1983).

- [53] G. A. Ermolaev, Y. V. Stebunov, A. A. Vyshnevyy, D. E. Tatarkin, D. I. Yakubovsky, S. M. Novikov, D. G. Baranov, T. Shegai, A. Y. Nikitin, A. V. Arsenin, and V. S. Volkov, *npj 2D Mater. Appl.* **4**, 21 (2020).
- [54] A. D. Yoffe, *Annu. Rev. Mater. Sci.* **3**, 147 (1973).
- [55] D. Kong, H. Wang, J. J. Cha, M. Pasta, K. J. Koski, J. Yao, and Y. Cui, *Nano Lett.* **13**, 1341 (2013).
- [56] C. Stern, S. Grinvald, M. Kirshner, O. Sinai, M. Oksman, H. Alon, O. E. Meiron, M. Bar-Sadan, L. Houben, and D. Naveh, *Sci. Rep.* **8**, 16480 (2018).
- [57] M. A. Islam, Ph.D. dissertation, University of Central Florida, 2019, electronic Theses and Dissertations, 6780.
- [58] A. B. Evlyukhin and B. N. Chichkov, *Phys. Rev. B* **100**, 125415 (2019).
- [59] S. Varault, B. Rolly, G. Boudarham, G. Demésy, B. Stout, and N. Bonod, *Opt. Express* **21**, 16444 (2013).
- [60] V. S. Asadchy, A. Díaz-Rubio, and S. A. Tretyakov, *Nanophotonics* **7**, 1069 (2018).
- [61] K. Achouri and O. J. F. Martin, *Phys. Rev. B* **104**, 165426 (2021).
- [62] A. B. Evlyukhin, M. A. Poleva, A. V. Prokhorov, K. V. Baryshnikova, A. E. Miroshnichenko, and B. N. Chichkov, *Laser Photonics Rev.* **15**, 2100206 (2021).
- [63] D. A. Bobylev, D. A. Smirnova, and M. A. Gorlach, *Phys. Rev. B* **102**, 115110 (2020).
- [64] A. B. Evlyukhin, C. Reinhardt, and B. N. Chichkov, *Phys. Rev. B* **84**, 235429 (2011).
- [65] I. Staude, A. E. Miroshnichenko, M. Decker, N. T. Fofang, S. Liu, E. Gonzales, J. Dominguez, T. S. Luk, D. N. Neshev, I. Brener *et al.*, *ACS Nano* **7**, 7824 (2013).
- [66] V. E. Babicheva and A. B. Evlyukhin, *J. Appl. Phys.* **129**, 040902 (2021).
- [67] A. E. Miroshnichenko, A. B. Evlyukhin, Y. S. Kivshar, and B. N. Chichkov, *ACS Photonics* **2**, 1423 (2015).
- [68] F. Lemarchand, private communications (2013), measurement method described in: L. Gao, F. Lemarchand, and M. Lequime, *Opt. Express* **20**, 15734 (2012).
- [69] J. W. Fleming, *Appl. Opt.* **23**, 4486 (1984).
- [70] E. Evlyukhin, E. Kim, P. Ciffigu, D. Goldberger, S. Schyck, B. Harris, S. Torres, G. R. Rossman, and M. Pravica, *J. Mater. Chem. C* **6**, 12473 (2018).
- [71] A. A. Popkova, I. M. Antropov, G. I. Tselikov, G. A. Ermolaev, I. Ozerov, R. V. Kirtaev, S. M. Novikov, A. B. Evlyukhin, A. V. Arsenin, V. O. Bessonov, V. S. Volkov, and A. A. Fedyanin, *Laser Photonics Rev.* **16**, 2100604 (2022).
- [72] U. Zywiets, M. K. Schmidt, A. B. Evlyukhin, C. Reinhardt, J. Aizpurua, and B. N. Chichkov, *ACS Photonics* **2**, 913 (2015).
- [73] S. Makarov, L. Kolotova, S. Starikov, U. Zywietze, and B. Chichkov, *Nanoscale* **10**, 11403 (2018).